

Magnon-Mediated Superconductivity in the Infinite- U Triangular Lattice

Hantian Zhu,¹ Yixin Zhang,¹ Shang-Shun Zhang,¹ Yang Zhang,^{1, 2, *} and Cristian D. Batista^{1, 3, †}

¹*Department of Physics and Astronomy, University of Tennessee, Knoxville, Tennessee 37996, USA*

²*Min H. Kao Department of Electrical Engineering and Computer Science,*

University of Tennessee, Knoxville, Tennessee 37996, USA

³*Neutron Scattering Division, Oak Ridge National Laboratory, Oak Ridge, TN, USA*

We demonstrate that the infinite- U triangular-lattice Hubbard model supports a superconducting state built from tightly bound Cooper pairs composed of two holes and one magnon ($2h1m$). Building on the seminal prediction of repulsively bound $2h1m$ states, we show that next-nearest-neighbor hopping t_2 coherently mixes symmetry-related configurations, stabilizing an s -wave bound state with substantial binding energy and a light effective mass. Large-scale DMRG calculations at finite doping identify a magnetization plateau corresponding to a gas of such bound states and quasi-long-range superconducting order with power-law $2h1m$ pair correlations. Our results establish a magnon-mediated superconducting mechanism driven by kinetic frustration, with immediate detectable signatures for moiré Hubbard materials and ultracold-atom simulators.

A central challenge in condensed matter physics is to understand how unconventional superconductivity (SC) can emerge from purely short-range *repulsive* interactions, as exemplified by the Hubbard model [1–5]. While conventional approaches invoke the exchange of virtual spin fluctuations to mediate pairing between fermions, here we explore a more radical mechanism: the formation of composite bosons in which magnetic excitations are physically bound to charge carriers. In this scenario, mobile carriers strongly reorganize the surrounding magnetic background, and the resulting many-body dressing can generate emergent effective attractions, even in the absence of any bare attractive interaction.

Recent advances in ultracold-atom quantum simulators and transition-metal dichalcogenide (TMD) moiré heterostructures have turned the Hubbard model into a highly tunable experimental platform [6–14]. These systems have enabled direct observation of long-standing theoretical predictions, including Nagaoka-type kinetic ferromagnetism and antiferromagnetic AFM spin-polaron formation [15–20]. In square-lattice realizations, a single doped carrier produces a pronounced distortion of AFM correlations, forming a magnetic “cloud” [21]. Upon doping a magnetic insulator, the magnon excitations themselves are likewise strongly renormalized by itinerant carriers, giving rise to magnetic polarons [22].

Frustration further enriches this physics. In the triangular-lattice Hubbard model at large U/t , hole doping enhances antiferromagnetic correlations [23], whereas electron doping produces extended ferromagnetic “bubbles” [24–26]. This pronounced particle-hole asymmetry originates from the fact that single-hole motion is *kinetically frustrated* on a ferromagnetic background, while single-electron motion is not. The frustration can be locally relieved when the two spins forming a triangle with the hole bind into a singlet state. This simple mechanism not only accounts for kinetically induced antiferromagnetism on frustrated lattices, but also underlies a growing class of unconventional states in doped Mott

insulators, including spin polarons [19, 27], resonating-valence-bond states on corner-sharing lattices [28], and frustration-driven pairing phenomena [19, 20, 29].

In triangular moiré heterostructures such as $\text{MoTe}_2/\text{WSe}_2$, recent optical studies [30, 31] have observed the predicted bound state of a hole and a flipped spin (relative to full spin polarization) with total spin $S = 3/2$ [19]. In this spin-polaron state, the magnon localizes on a triangle shared with the hole and forms a singlet with the neighboring spins, effectively reversing the sign of the local hopping amplitude (equivalent to a π flux) and thereby relieving kinetic frustration. A particularly clear experimental signature of a Fermi gas of such $S = 3/2$ polarons is the emergence of a magnetization plateau at $M = (1 - 3\delta)/2$, corresponding to one spin flip per doped hole, as observed in moiré bilayers [30] and in quantitative agreement with theoretical predictions [27].

As shown in Ref. [19], this mechanism can be extended further: a single magnon can bind two holes into a composite Cooper pair when carrier motion is sufficiently frustrated, for instance by including a third-neighbor hopping t_3 . Subsequent theoretical work demonstrated that a second-neighbor hopping t_2 provides an even more effective route to stabilizing the two-hole-one-magnon ($2h1m$) bound state in the triangular-lattice Hubbard model [20]. This three-body composite can be viewed as a spin polaron that captures an additional hole, providing a concrete example of how the coupling between charge motion and local magnetism can generate effective attraction from purely repulsive interactions. These results naturally raise the question: *Can moiré or ultracold-atom realizations of the Hubbard model be tuned into a regime where such $2h1m$ pairs proliferate and condense, giving rise to a magnon-mediated superconducting phase?*

Using density matrix renormalization group (DMRG) simulations at finite hole doping δ [32], we demonstrate the stability of a dilute gas of $2h1m$ quasiparticles. This regime is signaled by the emergence of a magnetization plateau at $M_p = (1 - 2\delta)/2$, corresponding to one spin flip

per pair of holes, and is characterized by quasi-long-range superconducting order of the composite Cooper pairs. While $2h1m$ pair-pair correlations decay as a power law, correlations of bare two-hole pairs remain short-ranged, unambiguously establishing that the magnon is not merely a mediator of attraction but an essential constituent of the Cooper pair itself.

We consider the infinite- U Hubbard model on a triangular lattice with nearest-neighbor (NN) hopping t_1 and next-nearest-neighbor (NNN) hopping t_2 in the presence of an external magnetic field $\mathbf{H} = H\hat{z}$:

$$\mathcal{H} = -t_1 \sum_{\langle ij \rangle \sigma} c_{i\sigma}^\dagger c_{j\sigma} - t_2 \sum_{\langle\langle ij \rangle\rangle \sigma} c_{i\sigma}^\dagger c_{j\sigma} + U \sum_i n_{i\uparrow} n_{i\downarrow} - h \sum_i S_i^z, \quad (1)$$

where $h = g\mu_B H$, μ_B is the Bohr magneton, g is the gyromagnetic factor and $\langle ij \rangle$ ($\langle\langle ij \rangle\rangle$) denotes NN (NNN) bonds ij .

We begin by considering the two-hole problem in the magnetic-field window where the ground state has $S^z \equiv \sum_i S_i^z = N/2 - 2$, corresponding to a fully polarized background with a single spin flip. Building on the analysis of Nazaryan and Fu [20], we revisit the two-hole-one-magnon ($2h1m$) bound state, which appears over a finite field range for $t_2/t_1 \gtrsim 0.09$. For $t_2/t_1 \gtrsim 0.15$, two such quasiparticles repel each other, indicating the stability of a dilute gas of $2h1m$ composites. Motivated by these results, we set $t_1 = 1$ and $t_2 = 0.3$ and perform exact diagonalization on a 12×12 lattice with periodic boundary conditions in both directions. The ground-state wave function in the $2h1m$ sector is obtained using the QuSpin package [33]. We then analyze the spatial structure of the bound state by fixing the positions of the two holes and evaluating the wave function as the magnon is moved across the lattice:

$$\psi(k | i, j) = \langle \Psi_G | c_{j\uparrow} c_{i\uparrow} S_k^- | \text{FM}\uparrow \rangle \quad S_k^- = c_{k\downarrow}^\dagger c_{k\uparrow} \quad (2)$$

Here k denotes the position of the mobile magnon, and i, j are the fixed positions of the two holes. The ground-state wave functions for three representative hole configurations are shown in Fig. 1. As the hole-hole separation increases from nearest neighbor to next-nearest neighbor and then to the farthest distance on the lattice, the magnon probability distribution evolves from strongly localized to progressively more delocalized, while the overall magnitude $|\psi(k; i, j)|$ decreases. This trend indicates the formation of a tightly bound three-body pair in which the two holes and the magnon cluster closely together.

To characterize the three-body bound state more explicitly, we introduce a real-space pair-creation operator that generates a $2h1m$ configuration on the fully polarized reference state $|\text{FM}\uparrow\rangle$:

$$\hat{\Delta}_{\hat{\mathbf{r}}_1, \hat{\mathbf{r}}_2, (x, y)} \equiv c_{(x, y) + \hat{\mathbf{r}}_1\uparrow} c_{(x, y) + \hat{\mathbf{r}}_2\uparrow} S_{(x, y)}^-, \quad (3)$$

where (x, y) denotes the magnon position and $\hat{\mathbf{r}}_{1,2}$ are the displacement vectors from the magnon to the two holes.

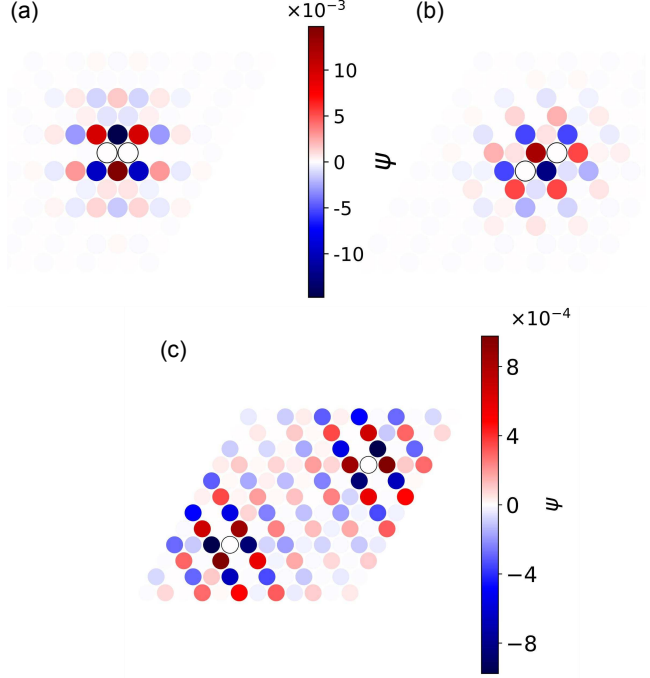


FIG. 1. Ground-state wave function from 12×12 ED for $t_1 = 1, t_2 = 0.3$ with the two hole positions fixed at: (a) a NN bond; (b) a NNN bond; (c) the maximal separation allowed by periodic boundary conditions.

By rotating this operator on the triangular lattice and tracking the phase acquired under C_6 transformations, we find that the bound state transforms trivially and therefore possesses s -wave symmetry.

To illustrate this symmetry, we focus on the two geometries with the largest amplitudes in Fig. 1: (i) a nearest-neighbor (NN) configuration in which the two holes and the magnon are mutually at nearest-neighbor separation, and (ii) a next-nearest-neighbor (NNN) configuration in which the holes are next-nearest neighbors, while each remains at nearest-neighbor separation from the magnon. Fixing the magnon at $(0, 0)$ and placing the holes on the corresponding sites, we compute the wave function under lattice rotations. As shown in Fig. 2, both configurations transform trivially under these rotations, confirming the s -wave character of the bound state.

The connectivity of the pairing geometries is governed by the hopping processes. For the dominant NN configuration, states related by a C_6 rotation of $\pi/3$ are connected by a single t_2 hop of one hole; likewise, NNN configurations related by a C_3 rotation of $2\pi/3$ are also linked by a single t_2 hop. Nearest-neighbor hopping t_1 further connects NN and NNN geometries. Consequently, the entire pairing manifold is connected through combinations of t_1 and t_2 processes, promoting coherent superposition of symmetry-related states, lowering the total energy, and stabilizing a finite binding energy,

$$E_b \equiv E(1h1m) + E(1h) - E(2h1m) \simeq 0.30, \quad (4)$$

for $t_1 = 1$ and $t_2 = 0.3$.

In the Supplemental Material (SM) we compute the $2h1m$ dispersion using the Lippmann–Schwinger equation and extract the corresponding effective mass. For $t_2 = 0.3$, the effective mass m^* is substantially reduced compared to $t_2 = 0.16$, enhancing the mobility of the bound pairs. In the dilute limit, essentially all composites participate in the condensate, so that the superfluid density satisfies $n_s \simeq \delta/2$ (density of hole pairs). The reduced effective mass therefore leads to an enhanced phase stiffness, $\rho_s \sim (\delta/2)/m^*$, favoring SC.

Motivated by these observations, we perform DMRG simulations using ITensor [34] for finite hole density δ at $t_1 = 1, t_2 = 0.3$. We study a 24×4 cylindrical geometry with open boundaries along \hat{x} and compute the magnetization M as a function of h for several values of δ at low temperature $k_B T = 0.03t_1$. The calculations employ a maximum bond dimension of 8000 and a truncation cutoff of 10^{-6} .

Upon lowering the magnetic field h from above saturation, we observe a broad magnetization plateau at incomplete polarization (see Fig. 3). By comparing the measured magnetization with the value expected for a dilute gas of $2h1m$ quasiparticles, $M_p = (1 - 2\delta)/2$, we identify this plateau as a phase stabilized by a finite density of $2h1m$ bound states [Fig. 3(a)]. Fixing the hole density to $\delta = 1/12$ and varying the system length L_x on an $L_x \times 4$ cylindrical geometry, we find that the resulting magnetization curves $M(h)$ are essentially independent of L_x [Fig. 3(b)]. This robustness establishes a controlled starting point for exploring unconventional superconductivity emerging from this phase.

The primary diagnostic of superconducting order is the SC pair–pair correlation function [35–41], defined as

$$\Phi(r)_{\hat{\mathbf{r}}_1, \hat{\mathbf{r}}_2, \hat{\mathbf{r}}_3, \hat{\mathbf{r}}_4} \equiv \langle \hat{\Delta}_{\hat{\mathbf{r}}_1, \hat{\mathbf{r}}_2, (x, y)}^\dagger \hat{\Delta}_{\hat{\mathbf{r}}_3, \hat{\mathbf{r}}_4, (x+r, y)} \rangle. \quad (5)$$

Each three-body pair operator $\hat{\Delta}_{\hat{\mathbf{r}}_1, \hat{\mathbf{r}}_2, (x, y)}^\dagger$ and $\hat{\Delta}_{\hat{\mathbf{r}}_3, \hat{\mathbf{r}}_4, (x+r, y)}$ represents a triangular unit composed of two holes and one magnon, while r denotes the separation between the two triangular units along the \hat{x} direction. To suppress boundary effects, we choose the reference position at $x = L_x/4$ and $y = L_y/2$.

In 1D systems, true long-range superconducting order is ruled out by the Mermin–Wagner theorem [42]. Quite generally, only quasi-long-range order is possible, with the pair–pair correlations decaying as a power-law with distance r : $\Phi(r) \sim r^{-K_{\text{sc}}}$. We focus on translationally related pair–pair correlations built from (i) a pair of parallel NN pairs with displacement vectors $\hat{\mathbf{r}}_1 = \hat{\mathbf{r}}_3 = (1, 0)$ and $\hat{\mathbf{r}}_2 = \hat{\mathbf{r}}_4 = (\frac{1}{2}, -\frac{\sqrt{3}}{2})$, and (ii) a pair of parallel NNN pairs with $\hat{\mathbf{r}}_1 = \hat{\mathbf{r}}_3 = (1, 0)$ and $\hat{\mathbf{r}}_2 = \hat{\mathbf{r}}_4 = (-\frac{1}{2}, -\frac{\sqrt{3}}{2})$. Using DMRG, we solve the Hubbard model with the magnetic field tuned to the multi- $2h1m$ magnetization plateau and

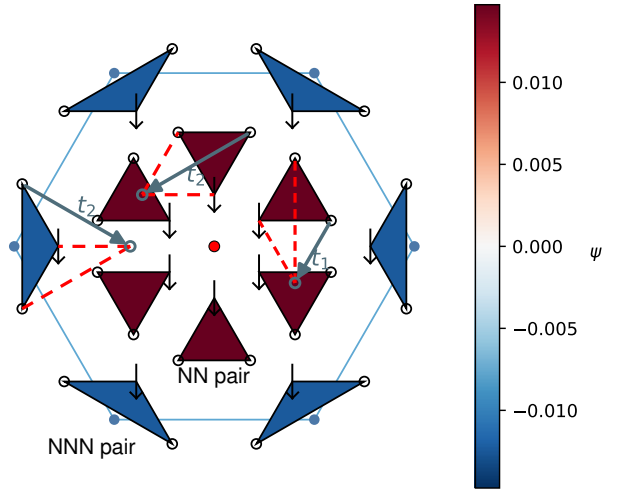


FIG. 2. The state map of the six NN and six NNN hole pairs (located at the blue markers) surrounding a fixed magnon at the center (red marker) reveals that the pairing manifold intrinsically possesses s –wave symmetry. Moreover, the next-nearest-neighbor hopping t_2 enables transitions between symmetry-related NN configurations as well as between symmetry-related NNN configurations, while the nearest-neighbor hopping t_1 connects a NN pair to a NNN pair.

study a $L_x \times 6$ cylinder with $L_x = 32$ at doping $\delta = 1/12$ (maximum bond dimension $m = 15,000$) and a $L_x \times 4$ cylinder at $\delta = 1/8$ ($m = 12,000$). Convergence of numerical results as a function of bond dimension is shown in the SM.

The resulting $\Phi(r)$ shown in Figs. 4(a,b) exhibit power-law decay $\Phi(r) \sim r^{-K_{\text{sc}}}$, with exponents $K_{\text{sc}} \simeq 1.37$ and 1.33 for NN and NNN pairs on the six-leg cylinder at $\delta = 1/12$, well as $K_{\text{sc}} \simeq 1.70$ and 1.68 for NN and NNN pairs on the four-leg cylinder at $\delta = 1/8$. This behavior is characteristic of a Luther–Emery (spin-gapped) regime in quasi-1D, wherein superconducting correlations display power-law decay while transverse spin correlations are short-ranged [43–46]. In all cases $K_{\text{sc}} < 2$, implying a superconducting susceptibility $\chi_{\text{sc}} \sim T^{-(2-K_{\text{sc}})}$ [45, 46] that diverges as $T \rightarrow 0$, consistent with the quasi-long-range superconducting order. The near equality of K_{sc} for NN and NNN pairs within the same system further suggests a unified quasi-long-range order even when the Cooper pairs possess real-space dispersion.

We also examine pair–pair correlations constructed solely from a two-hole operator,

$$\Phi_{2h}(r) \equiv \langle \Delta_{(x, y)}^\dagger \Delta_{(x+r, y)} \rangle, \quad (6)$$

where $\Delta_{(x, y)} \equiv c_{(x, y)\uparrow} c_{(x, y)+\hat{\mathbf{e}}\uparrow}$ creates a nearest-neighbor hole pair with bond vector $\hat{\mathbf{e}} = (-\frac{1}{2}, \frac{\sqrt{3}}{2})$. To minimize boundary effects, we fix the reference position at $x = L_x/4, y = L_y/2$ and evaluate $\Phi_{2h}(r)$ on a six-leg cylinder at $\delta = 1/12$ and a four-leg cylinder at $\delta = 1/8$, both

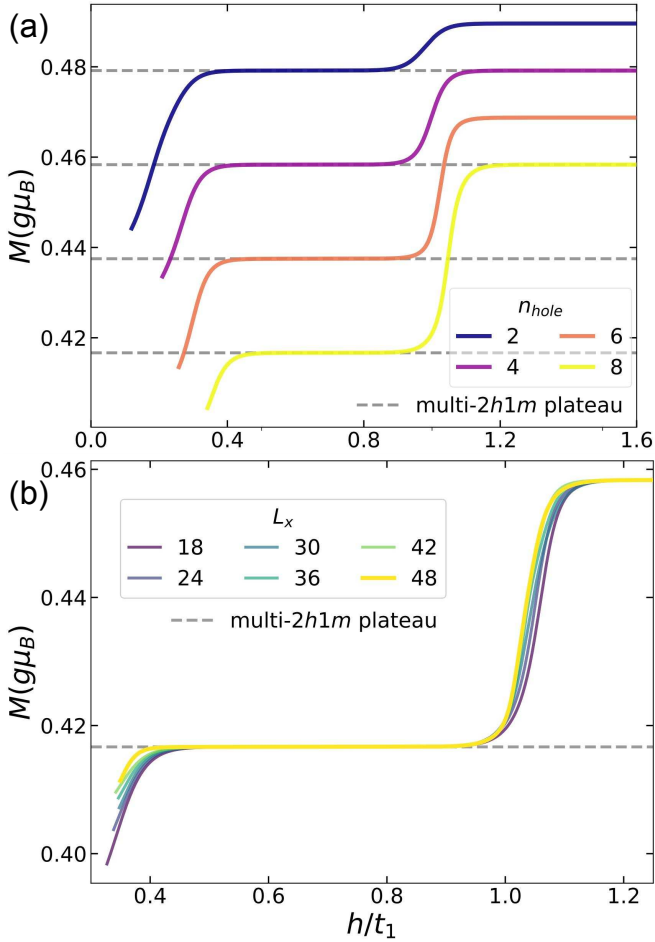


FIG. 3. Magnetization M as a function of magnetic field h on four-leg cylinders at low temperature $k_B T = 0.03t_1$: (a) for several number of hole dopings up to $n_{\text{hole}} = 8$ at fixed length $L_x = 24$, and (b) for system lengths up to $L_x = 48$ at fixed doping $\delta = 1/12$. In both cases, a finite field window $0.5t_1 < h < t_1$ is observed in which the system is stabilized in the multi-2h1m bound-state regime.

with $L_x = 32$. As shown in Fig. 4(c), $\Phi_{2h}(r)$ decays exponentially, $\Phi_{2h}(r) \sim e^{-r/\xi_{\text{sc}}}$, with correlation lengths $\xi_{\text{sc}} \simeq 1.21$ (six-leg, $\delta = 1/12$) and $\xi_{\text{sc}} \simeq 1.43$ (four-leg, $\delta = 1/8$). The short correlation length demonstrates the absence of long-range superconducting order arising from two-hole pairs alone, indicating that the magnon is an essential constituent of the Cooper pair rather than a mere mediator that induces attraction between holes. The condensate is formed not by holes, but by composite 2h1m quasiparticles.

Since the ground state corresponds to a dilute gas of holes and magnons doped into a spin polarized background, the system retains overall net magnetization. To characterize its magnetic correlations, we compute the transverse spin–spin correlation function

$$F(r) \equiv \langle S^x(x, y) S^x(x+r, y) + S^y(x, y) S^y(x+r, y) \rangle, \quad (7)$$

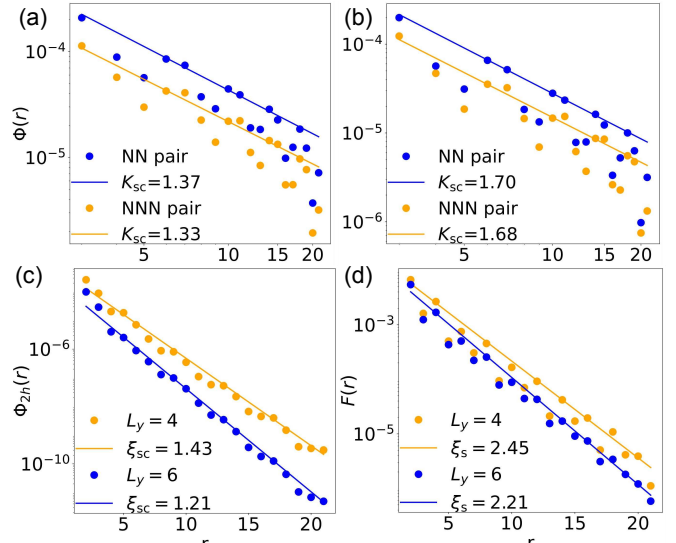


FIG. 4. NN and NNN pair–pair correlations $\Phi(r)$ plotted on double-logarithmic scales in (a) and (b) for the $N = 6 \times 32$, $\delta = 1/12$ (bond dimension $m = 15000$) and $N = 4 \times 32$, $\delta = 1/8$ (bond dimension $m = 12000$) cylinders, respectively. In both cases, $\Phi(r)$ follows a power-law decay, $\Phi(r) \sim r^{-K_{\text{sc}}}$. In contrast, the 2h-only pair correlations $\Phi_{2h}(r)$, shown on a semi-logarithmic scale in (c), decay exponentially, $\Phi_{2h}(r) \sim e^{-r/\xi_{\text{sc}}}$. The transverse spin–spin correlation $F(r)$, plotted on a semi-logarithmic scale in (d), also exhibits exponential decay, $F(r) \sim e^{-r/\xi_s}$.

evaluated at $x = L_x/4$ and $y = L_y/2$, and restricted to the transverse (x and y) spin components. For a six-leg cylinder at $\delta = 1/12$ and a four-leg cylinder at $\delta = 1/8$, the results shown in Fig. 4(d) exhibit exponential decay, $|F(r)| \sim e^{-r/\xi_s}$, with correlation lengths $\xi_s \simeq 2.43$ (six-leg, $\delta = 1/12$) and $\xi_s \simeq 2.46$ (four-leg, $\delta = 1/8$). The short-ranged nature of the transverse spin correlations reflects the competition between AFM tendencies and unconventional SC: by binding to hole pairs, magnons are prevented from condensing individually to form long-range AFM order.

From an experimental perspective, realizing magnon-mediated superconductivity in moiré or cold-atom Hubbard platforms would be highly significant, providing the first direct evidence of unconventional superconductivity emerging from strong repulsive interactions. As in the experimental observation of the predicted gas of $S = 3/2$ polarons [19, 27, 30], the magnetization plateau identified in this work offers a powerful diagnostic for characterizing this new state of matter. A key experimental challenge is to engineer a sizable next-nearest-neighbor hopping $t_2 \sim 0.3t_1$, which optimizes the binding energy E_b of the composite Cooper pairs. The value $E_b = 0.3t_1$ obtained in Eq. (4) is comparable to the binding energy $\simeq 0.5t_1$ of the $S = 3/2$ polarons in the absence of t_3 [19]. This suggests that the magnetization plateau reported here should become observable at temperatures comparable to

those at which the $S = 3/2$ polaron plateau was detected in moiré heterostructures [30, 31]. We further propose a targeted search in moiré homobilayers by sweeping the displacement field to modulate t_2/t_1 and stabilize the $2h1m$ state at intermediate doping.

As briefly illustrated in the Supplemental Material, the interplay between magnon-mediated superconductivity and competing charge- and spin-density-wave (CDW and SDW) tendencies warrants further investigation. More broadly, the unconventional pairing mechanism uncovered here can be generalized to a wide class of strongly correlated frustrated systems, offering a new route toward unconventional superconductivity beyond traditional paradigms.

Acknowledgments We thank Dr. Muqing Xu and Nianlong Zou for helpful discussions. Computations were performed on the group nodes and UTK ISAAC cluster. This work was supported by Max Planck partner lab grant on quantum materials. C.D.B. acknowledges support from the U.S. Department of Energy, Office of Science, Office of Basic Energy Sciences, under Award Number DE-SC0022311.

* yangzhang@utk.edu

† cbatist2@utk.edu

- [1] J. Hubbard, *Proceedings of the Royal Society of London. Series A* **276**, 238 (1963).
- [2] J. Kanamori, *Progress of Theoretical Physics* **30**, 275 (1963).
- [3] M. C. Gutzwiller, *Physical Review Letters* **10**, 159 (1963).
- [4] D. P. Arovas, E. Berg, S. A. Kivelson, and S. Raghu, *Annual Review of Condensed Matter Physics* **13**, 239 (2022).
- [5] P. A. Lee, N. Nagaosa, and X.-G. Wen, *Reviews of Modern Physics* **78**, 17 (2006).
- [6] F. Wu, T. Lovorn, E. Tutuc, and A. H. MacDonald, *Phys. Rev. Lett.* **121**, 026402 (2018).
- [7] Y. Zhang, N. F. Q. Yuan, and L. Fu, *Phys. Rev. B* **102**, 201115 (2020).
- [8] E. C. Regan, D. Wang, C. Jin, M. I. B. Utama, B. Gao, X. Wei, S. Zhao, W. Zhao, Z. Zhang, K. Yumigeta, M. Blei, J. D. Carlström, K. Watanabe, T. Taniguchi, S. Tongay, M. Crommie, A. Zettl, and F. Wang, *Nature* **579**, 359 (2020).
- [9] Y. Tang, L. Li, T. Li, Y. Xu, S. Liu, K. Barmak, K. Watanabe, T. Taniguchi, A. H. MacDonald, J. Shan, and K. F. Mak, *Nature* **579**, 353 (2020).
- [10] T. Li, S. Jiang, L. Li, Y. Zhang, K. Kang, J. Zhu, K. Watanabe, T. Taniguchi, D. Chowdhury, L. Fu, J. Shan, and K. F. Mak, *Nature* **597**, 350 (2021).
- [11] Y. Xu, K. Kang, K. Watanabe, T. Taniguchi, K. F. Mak, and J. Shan, *Nature Nanotechnology* **17**, 934 (2022).
- [12] R. Jördens, N. Strohmaier, K. Günter, H. Moritz, and T. Esslinger, *Nature* **455**, 204 (2008).
- [13] A. Mazurenko, C. S. Chiu, G. Ji, M. F. Parsons, M. Kanász-Nagy, R. Schmidt, F. Grusdt, E. Demler, D. Greif, and M. Greiner, *Nature* **545**, 462 (2017).
- [14] D. Greif, T. Uehlinger, G. Jotzu, L. Tarruell, and T. Esslinger, *Science* **340**, 1307 (2013).
- [15] Y. Nagaoka, *Phys. Rev.* **147**, 392 (1966).
- [16] J. O. Haerter and B. S. Shastry, *Phys. Rev. Lett.* **95**, 087202 (2005).
- [17] C. N. Sposetti, B. Bravo, A. E. Trumper, L. O. Manuel, and C. J. Gazza, *Phys. Rev. Lett.* **112**, 187204 (2014).
- [18] M. Davydova, Y. Zhang, and L. Fu, *Phys. Rev. B* **107**, 224420 (2023).
- [19] S.-S. Zhang, W. Zhu, and C. D. Batista, *Physical Review B* **97**, 140507 (2018), arXiv:1711.03233 [cond-mat.str-el].
- [20] K. G. Nazaryan and L. Fu, *Science Advances* **10**, eadp5681 (2024), <https://www.science.org/doi/pdf/10.1126/sciadv.adp5681>.
- [21] J. Koepsell, J. Vijayan, P. Sompé, F. Grusdt, T. A. Hilker, E. Demler, G. Salomon, I. Bloch, and C. Gross, *Nature* **572**, 358 (2019).
- [22] M. L. Prichard, Z. Ba, I. Morera, B. M. Spar, D. A. Huse, E. Demler, and W. S. Bakr, *Nature Physics* **21**, 1548 (2025).
- [23] J. O. Haerter and B. S. Shastry, *Physical Review Letters* **95**, 087202 (2005).
- [24] M. Prichard, B. Spar, I. Morera, E. Demler, Z. Yan, and W. S. Bakr, *Nature* **629**, 323–328 (2024).
- [25] M. Xu, L. H. Kendrick, A. Kale, Y. Gang, G. Ji, R. T. Scalettar, M. Lebrat, and M. Greiner, *Nature* **620**, 971 (2023).
- [26] M. Lebrat, M. Xu, L. H. Kendrick, A. Kale, Y. Gang, P. Seetharaman, I. Morera, E. Khatami, E. Demler, and M. Greiner, *Nature* **629**, 317 (2024).
- [27] Y. Zhang and L. Fu, *SciPost Phys. Core* **6**, 038 (2023).
- [28] C. Glittum, A. Štrkalj, D. Prabhakaran, P. A. Goddard, C. D. Batista, and C. Castelnovo, *Nature Physics* **21**, xxx (2025).
- [29] Y. Zhang, C. D. Batista, and Y. Zhang, *Antiferromagnetism and tightly bound cooper pairs induced by kinetic frustration* (2025), arXiv:2506.16464 [cond-mat.str-el].
- [30] Z. Tao, B. Shen, W. Zhao, N.-C. Hu, T. Li, S. Jiang, L. Li, K. Watanabe, T. Taniguchi, A. H. MacDonald, J. Li, J. Shan, and K. F. Mak, *Nature Physics* **20**, 783 (2024).
- [31] L. Ciociaro, T. Smołński, I. Morera, A. Popert, M. Kroner, E. Demler, and A. İmamoğlu, *Nature* **623**, 509 (2023).
- [32] S. R. White, *Physical Review Letters* **69**, 2863 (1992).
- [33] P. Weinberg and M. Bükov, *SciPost Phys.* **2**, 003 (2017).
- [34] M. Fishman, S. R. White, and E. M. Stoudenmire, *SciPost Phys. Codebases*, 4 (2022), arXiv:2007.14822 [cond-mat.str-el].
- [35] F. Chen, F. D. M. Haldane, and D. N. Sheng, *Proceedings of the National Academy of Sciences* **122**, e2420963122 (2025), arXiv:2311.15092 [cond-mat.supr-con].
- [36] Y.-F. Jiang, T. P. Devereaux, and H.-C. Jiang, *Physical Review B* **109**, 085121 (2024), arXiv:2303.15541 [cond-mat.str-el].
- [37] S.-S. Gong, W. Zhu, and D. N. Sheng, *Physical Review Letters* **127**, 097003 (2021).
- [38] S. Jiang, D. J. Scalapino, and S. R. White, *Proceedings of the National Academy of Sciences* **118**, e2109978118 (2021).
- [39] Y.-F. Jiang, J. Zaanen, T. P. Devereaux, and H.-C. Jiang, *Physical Review Research* **2**, 033073 (2020), arXiv:1907.11728 [cond-mat.str-el].
- [40] H.-C. Jiang, Z. Y. W. Chen, T. P. Devereaux, and S. A. Kivelson, *Science* **365**, 1424 (2019).

- [41] H.-C. Jiang and S. A. Kivelson, Proceedings of the National Academy of Sciences **119**, e2109406119 (2022).
- [42] N. D. Mermin and H. Wagner, Phys. Rev. Lett. **17**, 1133 (1966).
- [43] A. Luther and V. J. Emery, Phys. Rev. Lett. **33**, 589 (1974).
- [44] F. D. M. Haldane, J. Phys. C: Solid State Phys. **14**, 2585 (1981).
- [45] J. Voit, Reports on Progress in Physics **58**, 977 (1995), arXiv:cond-mat/9510014.
- [46] T. Giamarchi, *Quantum Physics in One Dimension* (Oxford University Press, Oxford, 2004).

Supplemental Material for “Magnon-Mediated Superconductivity in the Infinite- U Triangular Lattice”

Hantian Zhu,¹ Yixin Zhang,¹ Shang-Shun Zhang,¹ Yang Zhang,^{1, 2, *} and Cristian D. Batista^{1, 3, †}

¹*Department of Physics and Astronomy, University of Tennessee, Knoxville, Tennessee 37996, USA*

²*Min H. Kao Department of Electrical Engineering and Computer Science,*

University of Tennessee, Knoxville, Tennessee 37996, USA

³*Neutron Scattering Division, Oak Ridge National Laboratory, Oak Ridge, TN, USA*

(Dated: February 9, 2026)

EFFECTIVE MASS OF THE $2h1m$ PAIR

To quantify the mobility of the composite $2h1m$ pair, we compute its dispersion using the Lippmann–Schwinger (LS) equation and extract the corresponding effective mass. The wave function for two holes and one magnon can be expressed as follows:

$$|\psi_{\mathbf{Q}}\rangle = \sum_{\mathbf{r}_1, \mathbf{r}_2} \psi_{\mathbf{Q}}(\mathbf{r}_1, \mathbf{r}_2) \frac{1}{\sqrt{N}} \sum_{\mathbf{R}} e^{i\mathbf{Q}\cdot\mathbf{R}} |\mathbf{R}, \mathbf{R} + \mathbf{r}_1, \mathbf{R} + \mathbf{r}_2\rangle. \quad (\text{S1})$$

Here \mathbf{R} is the position vector of the mobile magnon, $\mathbf{r}_{1,2}$ is the relative position vector of two holes with respect to the magnon, and N is the number of lattice sites. The fermionic statistics of holes implies $\psi_{\mathbf{Q}}(\mathbf{r}_1, \mathbf{r}_2) = -\psi_{\mathbf{Q}}(\mathbf{r}_2, \mathbf{r}_1)$. The $2h1m$ wave function with total momentum \mathbf{Q} can be Fourier transformed as a function of the relative position \mathbf{r} of one hole with respect to the magnon and the relative momentum \mathbf{p} of the other hole with respect to the magnon:

$$\psi_{\mathbf{Q}}(\mathbf{p}, \mathbf{r}) = \frac{1}{\sqrt{N}} \sum_{\mathbf{r}'} e^{-i\mathbf{p}\cdot\mathbf{r}'} \psi_{\mathbf{Q}}(\mathbf{r}', \mathbf{r}). \quad (\text{S1})$$

From this wavefunction representation of the three-body state, we obtain the Lippmann–Schwinger equation. First, we separate the Hamiltonian into the free-particle part and the interaction part:

$$\mathcal{H} = \mathcal{H}_0 + \mathcal{H}_{\text{int}}. \quad (\text{S2})$$

The free-particle Hamiltonian is:

$$\mathcal{H}_0 = \sum_{\mathbf{p}} \xi_{\mathbf{p}} c_{\mathbf{p}}^\dagger c_{\mathbf{p}} + \sum_{\mathbf{q}} \omega_{\mathbf{q}} b_{\mathbf{q}}^\dagger b_{\mathbf{q}}, \quad (\text{S3})$$

where c_p^\dagger creates a hole with momentum p and b_q^\dagger creates a magnon with momentum q . Since the magnon is immobile in the infinite- U Hubbard limit, $\omega_{\mathbf{q}} = 0$. We consider the triangular-lattice dispersion for nearest-neighbor hopping t_1 and next nearest neighbor hopping t_2 . After setting the lattice constant $a = 1$, and choosing the lattice vectors $\mathbf{a}_1 = (1, 0)$, $\mathbf{a}_2 = (\frac{1}{2}, \frac{\sqrt{3}}{2})$, we obtain the following expression for the dispersion relation:

$$\xi_{\mathbf{p}} = 2t_1 \left[\cos p_x + 2 \cos\left(\frac{p_x}{2}\right) \cos\left(\frac{\sqrt{3}p_y}{2}\right) \right] + 2t_2 \left[\cos\left(\sqrt{3}p_y\right) + 2 \cos\left(\frac{3p_x}{2}\right) \cos\left(\frac{\sqrt{3}p_y}{2}\right) \right]. \quad (\text{S4})$$

The interaction part of the Hamiltonian includes (i) processes in which the magnon hops from other sites to a site occupied by a hole, and (ii) an onsite energy term when the magnon and a hole reside on the same site:

$$H_{\text{int}} = \sum_v t_v \hat{O}_v + V \sum_{\mathbf{r}} n_{\mathbf{r}} m_{\mathbf{r}}, \quad (\text{S5})$$

where ν enumerates all the nearest and next-nearest neighbor bonds (see Fig.S1), $n_{\mathbf{r}} = 1 - c_{\mathbf{r}}^\dagger c_{\mathbf{r}}$ and $m_{\mathbf{r}} = b_{\mathbf{r}}^\dagger b_{\mathbf{r}}$ are the number operators of the holes and magnons at site \mathbf{r} , and V is taken as ∞ to enforce the hard-core constraint that forbids the magnon and a hole from occupying the same lattice site ($\mathbf{r} = 0$ in the relative coordinate). The operator \hat{O}_v acting on the quantum state basis $|\mathbf{Q}; \mathbf{p}, \mathbf{r}\rangle$ is nonzero if and only if \mathbf{r} equals to a nearest-neighbor or a next-nearest-neighbor hopping vector \mathbf{e}_v :

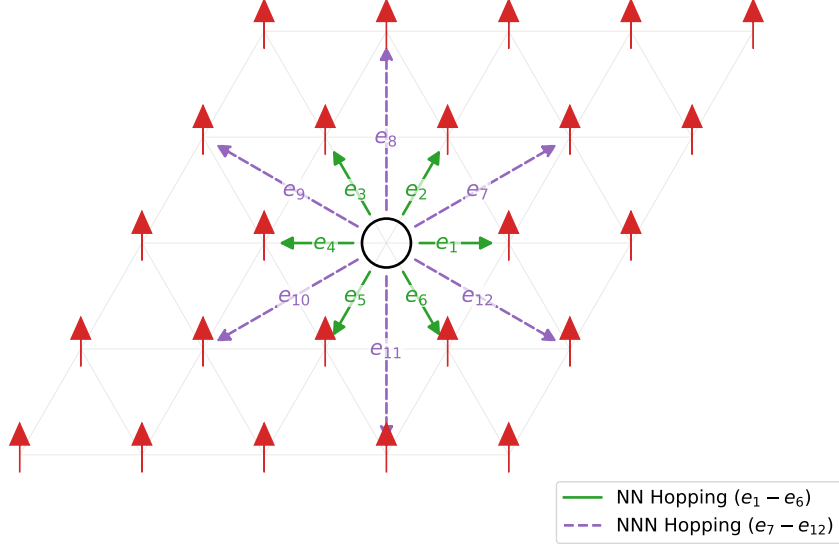


FIG. S1. The 6 nearest-neighbor hopping and 6 next-nearest hopping denoted by \mathbf{e}_v .

$$\hat{O}_v|\mathbf{Q}; \mathbf{p}, \mathbf{e}_v\rangle = e^{-i(\mathbf{Q}-\mathbf{p}) \cdot \mathbf{e}_v}|\mathbf{Q}; \mathbf{p}, -\mathbf{e}_v\rangle. \quad (\text{S6})$$

In this hard-core limit ($V \rightarrow \infty$), the physical wave function satisfies the boundary condition $\psi_{\mathbf{Q}}(\mathbf{p}, \mathbf{r} = \mathbf{0}) = 0$. Nevertheless, the product $V\psi_{\mathbf{Q}}(\mathbf{p}, \mathbf{0})$ entering the LS equation remains finite: $\psi_{\mathbf{Q}}(\mathbf{p}, \mathbf{0})$ scales as $1/V$ such that $V\psi_{\mathbf{Q}}(\mathbf{p}, \mathbf{0})$ approaches a finite contact scattering amplitude, which is determined self-consistently by the LS equation. For the bound state problem considered here, the LS equation reads as follows:

$$|\psi_{\mathbf{Q}}\rangle = G_0^{(3)}(E)\mathcal{H}_{\text{int}}|\psi_{\mathbf{Q}}\rangle \quad (\text{S7})$$

where

$$G_0^{(3)}(E) = \frac{1}{E - \mathcal{H}_0 + i\epsilon}. \quad (\text{S8})$$

We multiply $\langle \mathbf{Q}; \mathbf{p}, \mathbf{r} |$ from the left of both side, and get:

$$\psi_{\mathbf{Q}}(\mathbf{p}, \mathbf{r}) = \langle \mathbf{Q}; \mathbf{p}, \mathbf{r} | G_0^{(3)}(E) \mathcal{H}_{\text{int}} |\psi_{\mathbf{Q}}\rangle. \quad (\text{S9})$$

Using the matrix elements of \mathcal{H}_{int} under the quantum basis $|\mathbf{Q}; \mathbf{p}, \mathbf{r}\rangle$ derived above, we get the integral formula of $\psi_{\mathbf{Q}}(\mathbf{p}, \mathbf{r})$:

$$\begin{aligned} \psi_{\mathbf{Q}}(\mathbf{p}, \mathbf{r}) &= 2 \sum_v t_v \int \frac{d^2\mathbf{k}}{(2\pi)^2} G_{\mathbf{Q}_E}^{(3)}(\mathbf{p}, \mathbf{r}; \mathbf{k}, -\mathbf{e}_v) e^{-i(\mathbf{Q}-\mathbf{k}) \cdot \mathbf{e}_v} \psi_{\mathbf{Q}}(\mathbf{k}, \mathbf{e}_v) \\ &\quad + 2V \int \frac{d^2\mathbf{k}}{(2\pi)^2} G_{\mathbf{Q}_E}^{(3)}(\mathbf{p}, \mathbf{r}; \mathbf{k}, \mathbf{0}) \psi_{\mathbf{Q}}(\mathbf{k}, \mathbf{0}), \end{aligned} \quad (\text{S10})$$

$G_{\mathbf{Q}_E}^{(3)}$ is the non-interacting three-body Green's function of the non-interacting system:

$$\begin{aligned} G_{\mathbf{Q}_E}^{(3)}(\mathbf{p}_1, \mathbf{r}_1; \mathbf{p}_2, \mathbf{r}_2) &= \left\langle \mathbf{Q}; \mathbf{p}_1, \mathbf{r}_1 \left| \frac{1}{E - \mathcal{H}_0 + i\epsilon} \right| \mathbf{Q}; \mathbf{p}_2, \mathbf{r}_2 \right\rangle \\ &= 2\pi^2 \delta_{\mathbf{p}_1 \mathbf{p}_2} \int \frac{d^2\mathbf{k}}{(2\pi)^2} \frac{e^{-i\mathbf{k} \cdot (\mathbf{r}_2 - \mathbf{r}_1)}}{E - (\xi_{\mathbf{p}_2} + \xi_{\mathbf{k}} + \omega_{\mathbf{Q} - \mathbf{p}_2 - \mathbf{k}})} \\ &\quad - \frac{1}{2} \frac{e^{-i(\mathbf{p}_1 \cdot \mathbf{r}_2 - \mathbf{p}_2 \cdot \mathbf{r}_1)}}{E - (\xi_{\mathbf{p}_2} + \xi_{\mathbf{p}_1} + \omega_{\mathbf{Q} - \mathbf{p}_2 - \mathbf{p}_1})}. \end{aligned} \quad (\text{S11})$$

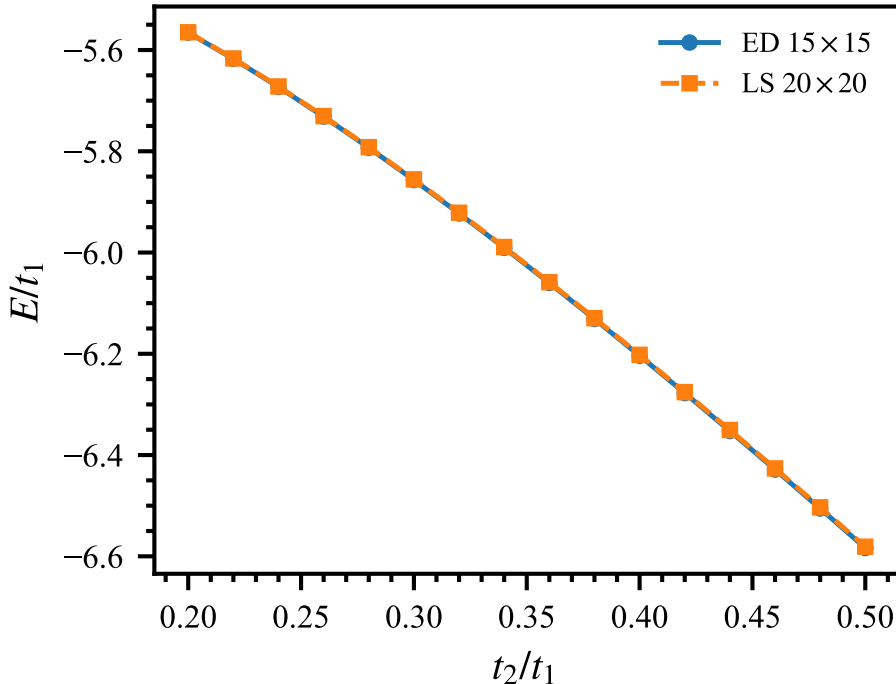


FIG. S2. Ground-state energy E of the $2h1m$ bound state as a function of the next-nearest-neighbor hopping t_2 , obtained from exact diagonalization (ED) on a 15×15 lattice (circles) and from the Lippmann–Schwinger (LS) equation evaluated on a 20×20 momentum grid (squares). The two methods show excellent agreement over the entire range of t_2 .

The hard-core constraint implies that at $\mathbf{r} = \mathbf{0}$:

$$0 = 2 \sum_v t_v \int \frac{d^2\mathbf{k}}{(2\pi)^2} G_{QE}^{(3)}(\mathbf{p}, \mathbf{0}; \mathbf{k}, -\mathbf{e}_v) e^{-i(\mathbf{Q}-\mathbf{k}) \cdot \mathbf{e}_v} \psi_{\mathbf{Q}}(\mathbf{k}, \mathbf{e}_v) + 2V \int \frac{d^2\mathbf{k}}{(2\pi)^2} G_{QE}^{(3)}(\mathbf{p}, \mathbf{0}; \mathbf{k}, \mathbf{0}) \psi_{\mathbf{Q}}(\mathbf{k}, \mathbf{0}). \quad (\text{S12})$$

The momentum integral over the first Brillouin zone in the LS equation is computed through the Gaussian quadrature method. Specifically, we replace the integral with by a discrete sum over Gaussian quadrature points,

$$\int_{\text{BZ}} \frac{d^2\mathbf{k}}{(2\pi)^2} F(\mathbf{k}) \approx \sum_{i,j=1}^n w_i w_j F(k_x^i, k_y^j),$$

where w_i denotes the weight at each Gaussian quadrature point and we take $n = 20$ in the calculations presented here. We compare the resulting ground-state energy with exact diagonalization (ED) on a 15×15 lattice for several values of t_2 . The LS energies are found to agree very well with the ED results over the entire parameter range considered as shown in the Fig. S2, indicating that the LS treatment reliably captures the low-energy $2h1m$ bound state.

We then vary the total momentum of the pair and obtain the full dispersion $E_{2h1m}(\mathbf{Q})$, from which the effective mass $m^*(t_2)$ is extracted from the curvature around the band minimum. Starting from $t_2 = 0.14t_1$, where the $2h1m$ bound state first becomes stable, and increasing t_2 up to $0.4t_1$, we find that m^* initially decreases rapidly and then continues to decrease more slowly at larger t_2 as shown in Fig. S3. The effective mass m^* is expressed in units of $\hbar^2/(t_1 a^2)$, where t_1 is the nearest-neighbor hopping amplitude and a is the lattice constant. This behavior shows that the composite pair becomes significantly lighter at sufficiently large t_2 , and therefore can move more easily through the ferromagnetic background, providing a more favorable environment for superconducting coherence. In particular, the relatively small effective mass when $t_2 = 0.3t_1$ offers a natural rationale for focusing on this t_2 value when demonstrating the presence of quasi-long-range superconducting order in the main text.

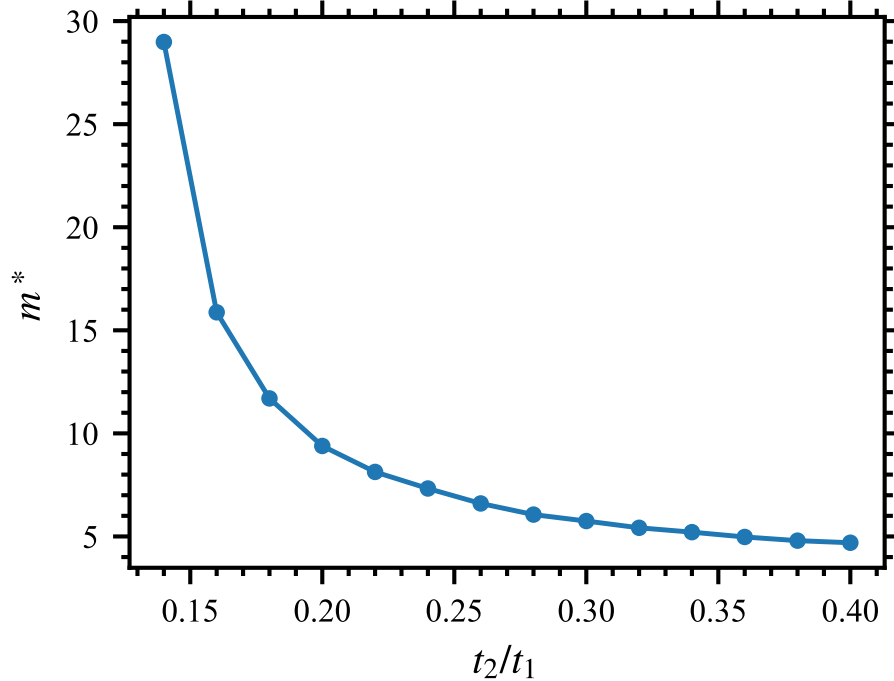


FIG. S3. Effective mass m^* of the 2h1m pair as a function of the next-nearest-neighbor hopping t_2 for $0.14 \leq t_2/t_1 \leq 0.40$. The effective mass decreases rapidly when t_2/t_1 is increased from 0.14, indicating that the composite pair becomes significantly lighter and more mobile at larger t_2 , which is favorable for the development of superconducting order.

CHARGE AND SPIN DENSITY WAVES

In quasi-one-dimensional geometries, there is a pronounced tendency toward charge-density-wave (CDW) order. Indeed, DMRG studies of doped square-lattice Hubbard models with next-nearest-neighbor hopping have shown that whenever quasi-long-range superconducting correlations emerge, sizable CDW modulations coexist [1], particularly for small cylinder circumferences L_y . This behavior reflects, on the one hand, the presence of Friedel oscillations induced by the open boundaries inherent to cylindrical geometries, and, on the other hand, the enhanced one-dimensional character, which suppresses superconducting correlations while favoring CDW order.

In our system, the situation is further enriched by the presence of both hole and magnon doping. The finite hole concentration naturally gives rise to charge oscillations and associated CDW patterns, while the finite density of magnons simultaneously induces oscillations in the longitudinal spin component S^z , leading to pronounced spin-density-wave (SDW) behavior. In this section, we analyze these numerical signatures of CDW and SDW order in detail.

We first examine the spatial profiles of the hole and magnon densities. To this end, we consider one-dimensional cuts along the x direction and define

$$n_h(r) = \langle 1 - \hat{n}_{(x_0+r,y_0)\uparrow} - \hat{n}_{(x_0+r,y_0)\downarrow} \rangle, \quad n_m(r) = \langle \hat{n}_{(x_0+r,y_0)\downarrow} \rangle,$$

where we choose a reference point at $x_0 = L_x/4$ and $y_0 = L_y/2$ and calculate for a six-leg cylinder at $\delta = 1/12$ and a four-leg cylinder at $\delta = 1/8$ (both with $L_x = 32$). The resulting hole density $n_h(r)$ and magnon density $n_m(r)$ are shown in Fig. S4 and Fig. S5, respectively. Both quantities exhibit oscillations as a function of r . In particular, the oscillation amplitude grows significantly as $x_0 + r$ approaches the open boundary, reflecting the strong boundary-induced modulations in this quasi-one-dimensional geometry. Moreover, the dominant oscillation period is approximately four lattice spacings, consistent with a characteristic wavelength set by L_y and the hole concentration δ . For small L_y , the bound pairs tend to distribute rather uniformly along the x direction, so that the density modulations naturally acquire a period of $2L_y/\delta$ in the x direction for the parameters considered here. This provides a simple explanation for the strong density oscillations observed along the cylinder, even in the presence of quasi-long-range superconducting correlations.

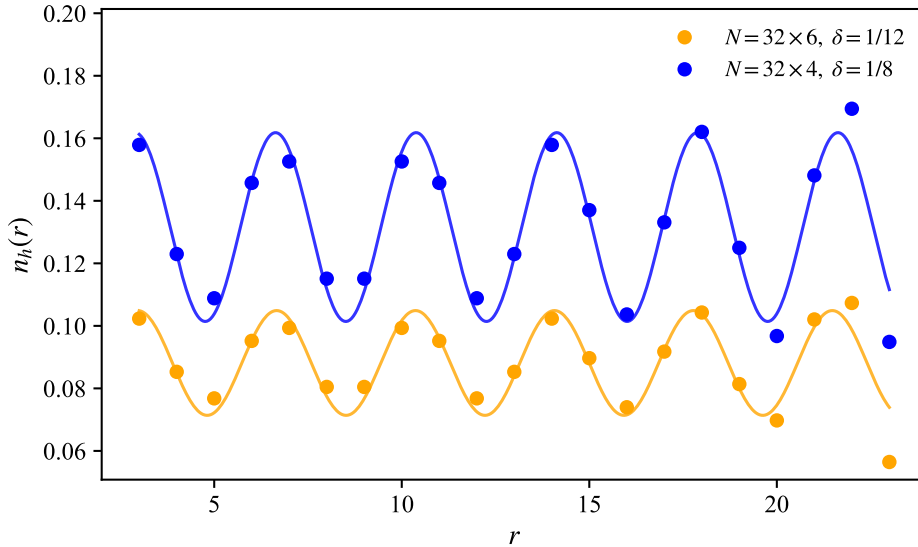


FIG. S4. Hole density profile $n_h(r)$ along the x direction on $L_x = 32$ cylinders with $L_y = 4$ (blue, $\delta = 1/8$) and $L_y = 6$ (orange, $\delta = 1/12$).

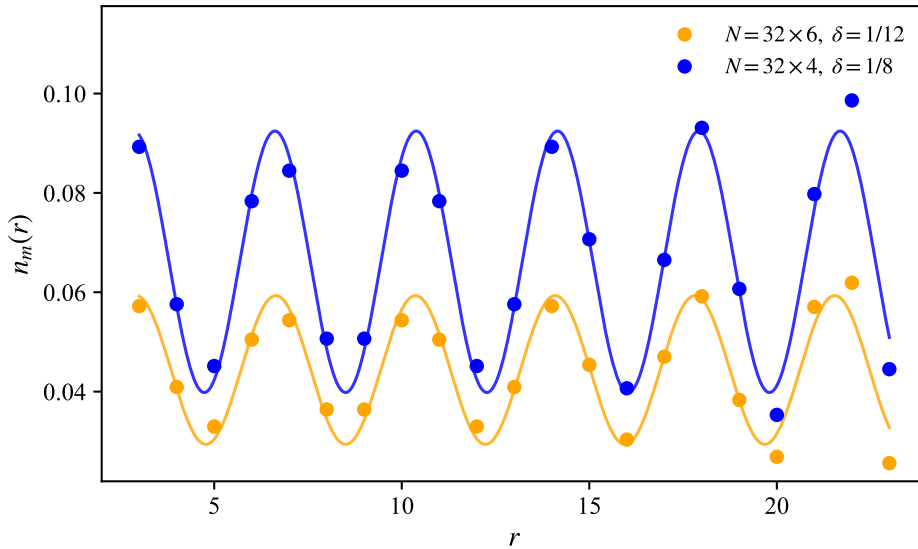


FIG. S5. Magnon density profile $n_m(r)$ along the x direction on cylindrical geometries with $L_x = 32$ and $L_y = 4$ (blue, $\delta = 1/8$) and $L_y = 6$ (orange, $\delta = 1/12$).

We also compute the charge density–density fluctuation correlation function on both lattices, defined as

$$D(r) = \langle (\hat{n}_{(x_0, y_0)} - n_{(x_0, y_0)}) (\hat{n}_{(x_0+r, y_0)} - n_{(x_0+r, y_0)}) \rangle, \quad (\text{S13})$$

where $n_{x_0, y_0} = \langle \hat{n}_{(x_0, y_0)} \rangle$ and $n_{(x_0+r, y_0)} = \langle \hat{n}_{(x_0+r, y_0)} \rangle$ denote the local average charge densities. As before, we fix the reference point at $x_0 = L_x/4$ and $y_0 = L_y/2$ and vary the separation r along the x direction. The resulting $D(r)$ exhibits a power-law decay with distance r : $D(r) \sim r^{-K_{\text{cdw}}}$, as shown in Fig. S6. Comparing the CDW exponent K_{cdw} extracted from $D(r)$ with the superconducting exponent K_{sc} obtained in the main text, we find that $K_{\text{sc}} > K_{\text{cdw}}$ on both cylinders. However, upon increasing the circumference from $L_y = 4$ to $L_y = 6$, K_{sc} decreases rapidly, whereas K_{cdw} exhibits a slight increase. This opposite trend suggests that, for wider cylinders with $L_y \sim 8$ or 12 , the quasi-one-dimensional constraint may be further relaxed, potentially leading to a regime in which superconducting correlations dominate over CDW correlations.

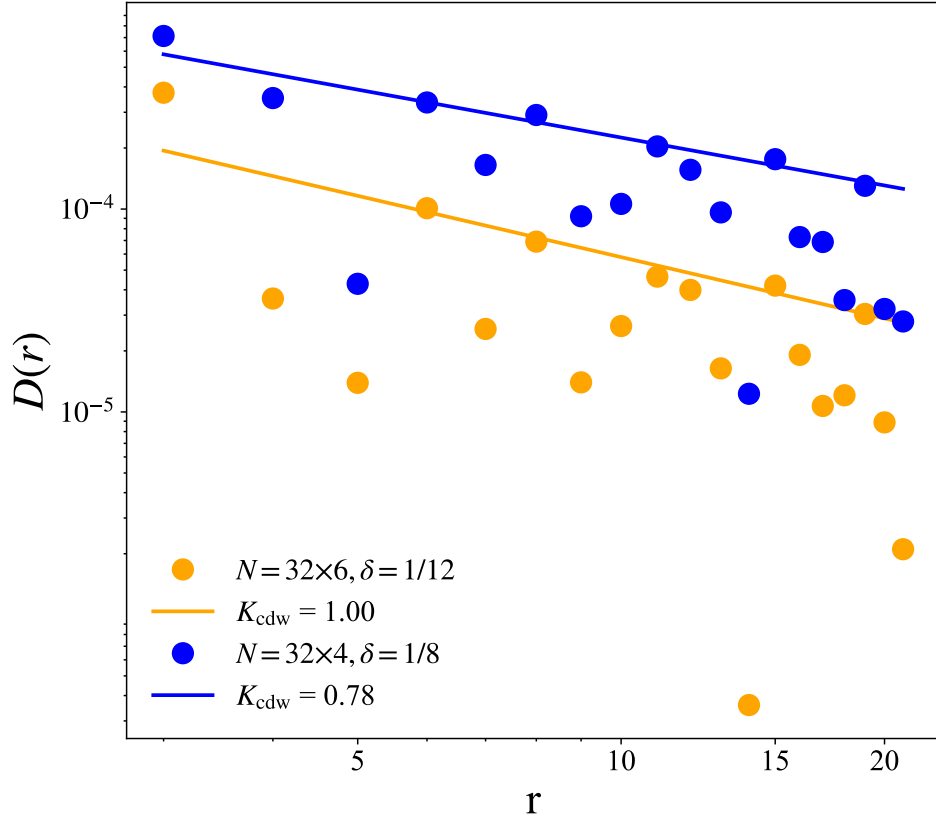


FIG. S6. Charge density-density correlation $D(r)$ plotted on double-logarithmic scales in (a) and (b) for the $N = 6 \times 32, \delta = 1/12$ (bond dimension $m = 15000$) and $N = 4 \times 32, \delta = 1/8$ (bond dimension $m = 12000$) cylinders, respectively, both follow power-law decay $\Phi(r) \sim r^{-K_{cdw}}$

On the other hand, the present model is purely kinetic-energy driven, with an infinite on-site repulsion (Hubbard $U = \infty$). If additional spin interactions of the t - J type are included, holes and magnons may further lower the spin interaction energy by forming bound pairs. Indeed, existing studies of the t - J model report robust quasi-long-range superconducting order without accompanying CDW order [2]. In the main text, we have deliberately focused on magnon-mediated superconductivity and its pairing mechanism as the central result of this work, while a more systematic analysis of the competition and coexistence among superconducting, CDW, and SDW orders is left for future investigation.

We similarly compute the longitudinal spin-density-wave (SDW) correlation function along the z direction, defined as

$$F_z(r) = \langle (\hat{S}_{(x_0, y_0)}^z - S_{(x_0, y_0)}^z)(\hat{S}_{(x_0+r, y_0)}^z - S_{(x_0+r, y_0)}^z) \rangle, \quad (\text{S14})$$

where $S_{(x_0, y_0)}^z = \langle \hat{S}_{(x_0, y_0)}^z \rangle$ and $S_{(x_0+r, y_0)}^z = \langle \hat{S}_{(x_0+r, y_0)}^z \rangle$ denote the local average magnetization along the z direction. As in the charge sector, we fix the reference point at $x_0 = L_x/4$ and $y_0 = L_y/2$, and vary the separation r along the x direction. The resulting $F_z(r)$ exhibits a power-law decay with distance r , $|F_z(r)| \sim r^{-K_{sdw}}$, as shown in Fig. S7.

We find that the longitudinal SDW correlations $F_z(r)$ exhibit behavior very similar to that of the CDW correlations $D(r)$ as a function of distance r . This similarity indicates that, in the present system, magnons play a role analogous to that of holes.

DETAILS OF THE DMRG CALCULATION

In this section, we briefly discuss technical aspects of the DMRG ground-state calculations. We employ the DMRG algorithm as implemented in the ITensor library [3] on finite cylindrical geometries. Compared with conventional

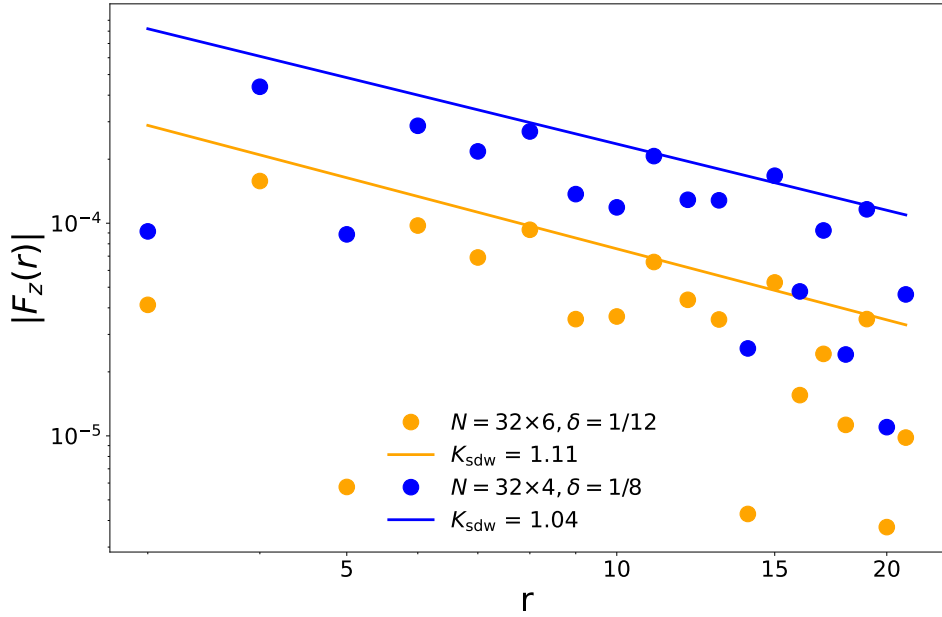


FIG. S7. The z -component of the spin–spin correlation function $|F_z(r)|$ plotted on double–logarithmic scales in (a) and (b) for the $N = 6 \times 32$, $\delta = 1/12$ (bond dimension $m = 15000$) and $N = 4 \times 32$, $\delta = 1/8$ (bond dimension $m = 12000$) cylinders, respectively. In both cases, the data follow a power-law decay $|F_z(r)| \sim r^{-K_{\text{sdw}}}$.

doped Hubbard or t – J models with nearest- and next-nearest-neighbor hopping on the square lattice, our multi- $2h1m$ system involves a very low density of magnons relative to the fully polarized background: the number of spin-down electrons is of order $\delta/2$, such that $N_\uparrow \gg N_\downarrow$. By contrast, most DMRG studies of superconductivity in doped Hubbard or t – J models on square lattices are performed in the total- $S^z = 0$ sector, starting from an antiferromagnetic parent state with $N_\uparrow \simeq N_\downarrow$. As a consequence, the Hilbert subspace explored in our simulations is substantially smaller than in the usual AFM-based setups.

Furthermore, we work in the infinite- U limit and explicitly forbid double occupancy, which further reduces the accessible Hilbert space. We study an $L_x \times 6$ cylinder with $L_x = 32$ at doping $\delta = 1/12$ using a maximum bond dimension of $m = 15,000$, and an $L_x \times 4$ cylinder at $\delta = 1/8$ with $m = 12,000$. For these parameters, the chosen bond dimensions are sufficient: the final DMRG truncation errors are as small as 3.61×10^{-8} for the six-leg cylinder at $\delta = 1/12$ and 1.92×10^{-9} for the four-leg cylinder at $\delta = 1/8$.

We have also verified convergence with respect to the bond dimension m for both lattice geometries. In addition to the largest bond dimensions quoted above, we performed DMRG calculations with a reduced bond dimension of $m = 8000$ and evaluated the nearest-neighbor superconducting pair–pair correlation functions using the same procedure as in the main text. As shown in Figs. S8 and S9, the resulting pair–pair correlators for $L_x \times 4$ at $\delta = 1/8$ and $L_x \times 6$ at $\delta = 1/12$ are almost indistinguishable from those obtained with $m = 12,000$ and $m = 15,000$, respectively. This demonstrates that our DMRG simulations are well converged with respect to the bond dimension and that the extracted quasi-long-range superconducting correlations are numerically robust.

* yangzhang@utk.edu

† cbatist2@utk.edu

[1] H.-C. Jiang, T. P. Devereaux, and S. A. Kivelson, arXiv:2511.18644 (2025), arXiv:2511.18644 [cond-mat.str-el].
 [2] F. Chen, F. D. M. Haldane, and D. N. Sheng, *Proceedings of the National Academy of Sciences* **122**, e2420963122 (2025), arXiv:2311.15092 [cond-mat.supr-con].
 [3] M. Fishman, S. R. White, and E. M. Stoudenmire, *SciPost Phys. Codebases* , 4 (2022), arXiv:2007.14822 [cond-mat.str-el].

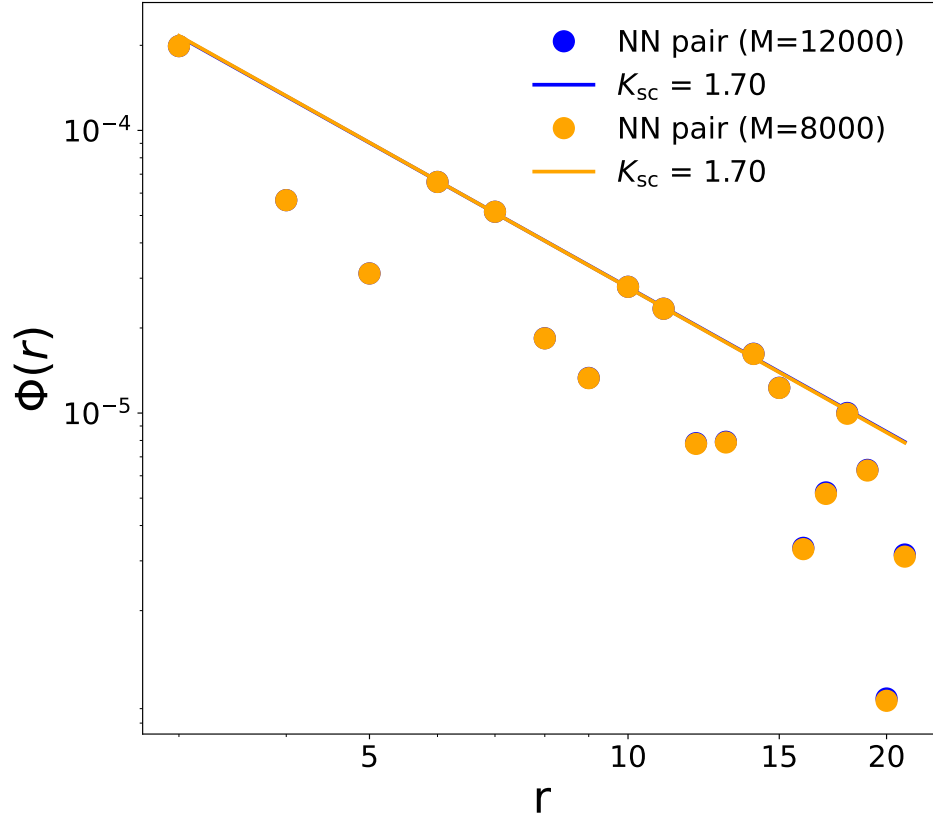


FIG. S8. The nearest-neighbor pair-pair correlation function on an $L_x = 32$ four-leg cylinder at doping $\delta = 1/8$ for two different maximum bond dimensions, $m = 12,000$ and $m = 8,000$. The two datasets are almost identical over the entire distance range, demonstrating that the DMRG results are well converged with respect to the bond dimension.

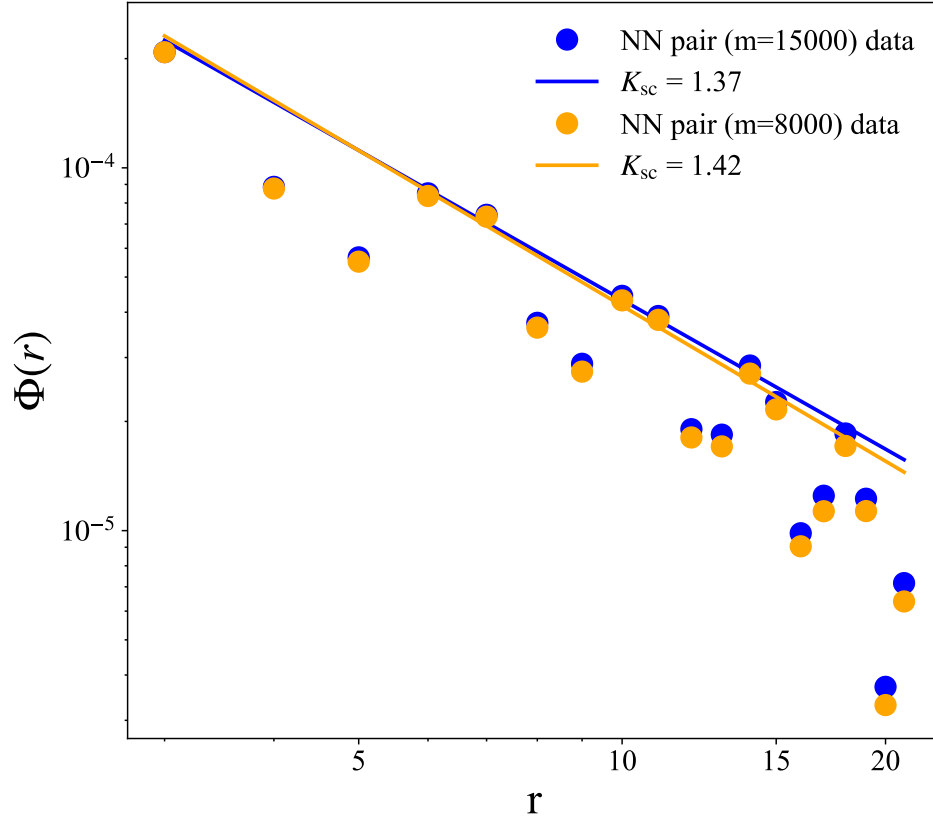


FIG. S9. The nearest-neighbor pair-pair correlation function on an $L_x = 32$ six-leg cylinder at doping $\delta = 1/12$ for two different maximum bond dimensions, $m = 15,000$ and $m = 8,000$. The two datasets are almost identical over the entire distance range, demonstrating that the DMRG results are well converged with respect to the bond dimension.